

Are Peak Summer Sultry Heat Wave Days over the Yangtze–Huaihe River Basin Predictable?

MIAONI GAO

Key Laboratory of Environmental Change and Natural Disaster, Ministry of Education, Beijing Normal University, and School of Systems Science, Beijing Normal University, Beijing, China

BIN WANG

Department of Atmospheric Sciences, and International Pacific Research Center, University of Hawai'i at Mānoa, Honolulu, Hawaii, and Earth System Modeling Center, Nanjing University of Information Science and Technology, Nanjing, China

JING YANG

State Key Laboratory of Earth Surface Processes and Resource Ecology, and Academy of Disaster Reduction and Emergency Management, and, Faculty of Geographical Science, Beijing Normal University, Beijing, China

WENJIE DONG

School of Atmospheric Sciences, Sun Yat-sen University, Guangdong, China

(Manuscript received 22 May 2017, in final form 20 October 2017)


ABSTRACT

The Yangtze–Huaihe River basin (YHRB) is the core region of sultry heat wave occurrence over China during peak summer [July and August (JA)]. The extremely hot and muggy weather is locally controlled by a descending high pressure anomaly connected to the western Pacific subtropical high. During 1961–2015, the heat wave days (HWDs) in JA over the YHRB exhibit large year-to-year and decadal variations. Prediction of the total number of HWDs in JA is of great societal and scientific importance. The summer HWDs are preceded by a zonal dipole SST tendency pattern in the tropical Pacific and a meridional tripole SST anomaly pattern over the North Atlantic. The former signifies a rapid transition from a decaying central Pacific El Niño in early spring to a developing eastern Pacific La Niña in summer, which enhances the western Pacific subtropical high and increases pressure over the YHRB by altering the Walker circulation. The North Atlantic tripole SST anomalies persist from the preceding winter to JA and excite a circumglobal teleconnection pattern placing a high pressure anomaly over the YHRB. To predict the JA HWDs, a 1-month lead prediction model is established with the above two predictors. The forward-rolling hindcast achieves a significant correlation skill of 0.66 for 1981–2015, and the independent forecast skill made for 1996–2015 reaches 0.73. These results indicate the source of predictability of summer HWDs and provide an estimate for the potential predictability, suggesting about 55% of the total variance may be potentially predictable. This study also reveals greater possibilities for dynamical models to improve their prediction skills.

1. Introduction

Heat waves (HWs) have gained wide attention among extreme weather events because they have widespread impacts on human health, society,

economy, and ecosystems (e.g., Easterling et al. 2000; National Academies of Sciences, Engineering, and Medicine 2016). Several studies have reported that the HW events in China increased in the recent decades (e.g., Ding and Ke 2015; You et al. 2016) and will occur with a higher frequency and longer duration in the future (IPCC 2013). Thus, there is a growing demand for improving HW prediction, especially the seasonal prediction of the total number of HW days (HWDs) in summer, the time scale of which is important for

 Denotes content that is immediately available upon publication as open access.

Corresponding author: J. Yang, yangjing@bnu.edu.cn

disaster prevention and mitigation and water resources management.

How skillful is the dynamical model's forecast of temperature over China in summer? Previous studies have found that the current dynamical models had low skills in predicting both seasonal mean and extremely high temperature over the Yangtze–Huaihe River basin (YHRB), which is the core region of sultry HW occurrence in China. For instance, Wang et al. (2009b) assessed the 1-month lead seasonal prediction skill of a multimodel ensemble (MME) performed by 14 dynamical models participating in the Climate Prediction and its Application to Society (CliPAS) for global summer 2-m air temperature in 1981–2003. They found that the YHRB exhibits extremely low temporal correlation coefficient scores of less than 0.1. According to the retrospective forecast from Met Office seasonal forecasting system and the ENSEMBLES project presented by Hamilton et al. (2012) and Pepler et al. (2015), the prediction skill of extremely high temperature days over YHRB in summer is similar to that of mean temperature. Furthermore, we evaluated the relevant performance of the dynamical model reforecast from the European Centre for Medium-Range Weather Forecasts (ECMWF), which participates in the Subseasonal-to-Seasonal (S2S) Prediction Project. The July–August-averaged correlation skill of the HWDs over the YHRB during 1995–2014 with observations is 0.28. The limited prediction skill of dynamical models motivates us to establish a physics-based empirical model (PEM) for HW forecasts.

Understanding the underlying causes of the interannual variability of HW is crucial for building the PEM. Plenty of studies have identified the factors contributing to the interannual variation of HWs in China, including the influence of summer soil moisture (Zhang and Wu 2011), North Atlantic Oscillation (Sun 2012), Tibetan Plateau snow cover (Wu et al. 2016), sea surface temperature (SST) over the Pacific Ocean (Zhou and Wu 2016), and winter–summer SST over the equatorial Indian Ocean and Pacific Ocean (Lei et al. 2009). However, the majority of these studies focused on the simultaneous connections between the climate variables and the HW event. For the YHRB, the source of predictability for sultry HWs on a seasonal time scale remains elusive.

Therefore, in this study, we attempt to answer two questions: 1) What is the source of predictability for summer HWDs total number over the YHRB? 2) To what extent could the interannual variability of HWDs over the YHRB be predicted? The rest of the paper is structured as follows. Section 2 introduces the datasets and methods used in the study. The definition of HWDs and the simultaneous atmospheric circulation associated

with HWDs are described in section 3. In section 4 we detect two SST predictors for the HWDs over the YHRB and explain the physical linkage between the predictors and predictand. In section 5, we establish a PEM to predict the HWDs and estimate its predictability. Finally, the summary and discussion are presented in section 6.

2. Data and methodology

a. Data

The newly released daily temperature dataset over China (CN05.1) from the National Climate Center in China with a high spatial resolution (0.25°) for the period 1961–2015 was used to depict the HWDs, including daily maximum temperature T_{\max} and relative humidity (Xu et al. 2009; Wu and Gao 2013). The monthly mean atmospheric circulation, 2-m air temperature, radiative flux, and total cloud cover were derived from the National Centers for Environmental Prediction (NCEP)–National Center for Atmospheric Research (NCAR) reanalysis datasets with a 2.5° spatial resolution and 17 pressure levels in the vertical for the same period (Kalnay et al. 1996; NOAA/OAR/ESRL PSD 1996). In addition, the monthly SST with a 2° spatial resolution was provided by the National Oceanic and Atmospheric Administration (NOAA) Extended Reconstructed SST (Huang et al. 2015).

The hindcasts of the model from ECMWF participating in the S2S Prediction Project during the period 1995–2014 were used to evaluate the performance of dynamical model (Vitart et al. 2015, 2017). The reforecasts of July and August were initiated from 15 June and 16 July, respectively, which yielded 15-day lead forecasts. The HWDs were made by averaging the results derived from 10 perturbed forecasts. Since the relative humidity is not available, the HWDs refer to the domain-averaged accumulated days with T_{\max} exceeding 35°C (Huang et al. 2010), which is different from the definition in section 3.

We focused on HWDs in July–August (JA) for two reasons. First, JA is the peak season of HWs characterized by high humidity over central-eastern China (Fig. 1a, also Ding and Ke 2015; Gao et al. 2018). Second, the northward migration of the western Pacific subtropical high (WPSH) in JA provides a robust large-scale circulation background for HW occurrence over YHRB (Wang et al. 2009a).

b. Methodology

Compared to a pure statistical model, a PEM is a new approach based on the understanding of physical linkages between the predictors and predictand.

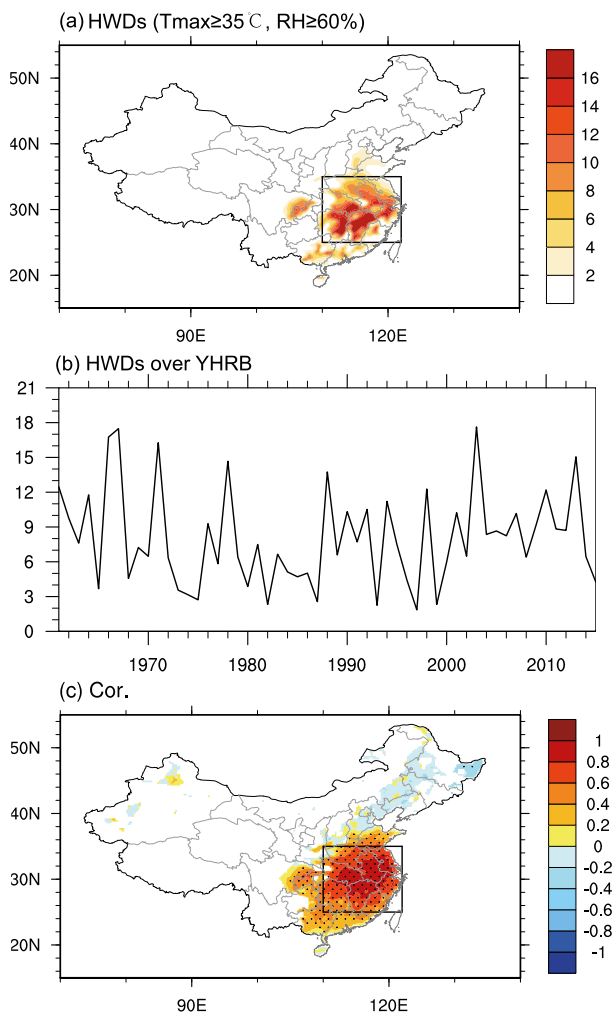


FIG. 1. (a) The 55 summer mean accumulated HWDs (days yr^{-1}) for each grid over China in JA during the period 1961–2015. (b) Time series of the accumulated HWDs averaged over the YHRB for 1961–2015. (c) The correlation map between the accumulated HWDs averaged over the YHRB and accumulated HWDs (days yr^{-1}) on each grid over China. The black rectangles in (a), (c) denote the YHRB. Black dots indicate where the results are significant at the 95% confidence level.

Correlation maps between a predictand and lower boundary variables are used to identify predictors that are physically connected to and significantly correlated with the predictand for the PEM in the training period (Wang et al. 2015). Since the monthly lower boundary variables have a significant trend in the past 55 years (figures not shown), which might be governed by different mechanisms from interannual variability such as anthropogenic forcing, the predictand and these lower boundary variables in each month have been detrended through removing the least squares linear trend of the time series to focus on the interannual variation of HWDs.

Three validation methods were chosen to estimate the predictability of the PEM. First, leave-three-out cross validation (Michaelsen 1987) was performed by building the regression function with three years removed from the training samples at each time step in 1961–2015 and the prediction was made for the central missing year. Second, a forward-rolling hindcast model was built with predictors obtained from a 20-yr training data period before the prediction year, and forecasts were made for the ensuing 10 years. For example, we built the first prediction model with the data during the training period of 1961–80 to predict HWDs from 1981 to 1990, and then built the second PEM with the data during the training period of 1971–90 to predict the HWDs in 1991–2000, and so on. Note the prediction function for each period is different because the training data are different. Third, an independent forecast was applied, in which the predictors were selected and the prediction model was established using the data from the training period from 1961 to 1995, and the JA HWDs during 1996–2015 were predicted. The prediction equation contains no “future” information in the independent forecast model (Wang et al. 2015). Note that the prediction skills of the PEM denote the correlation coefficients between the HWDs in the observation and hindcast.

3. Interannual variation of HWDs over the YHRB

a. Definition of HWDs

Several reasonable indices have been proposed to identify HWs through setting a local threshold temperature in a certain region (e.g., Anderson and Bell 2011; Smith et al. 2013; Teng et al. 2013; Wu et al. 2016). Since HWs over YHRB in JA are characterized by not only extremely high temperature but also high humidity that differs from the “dry” HW events in northwestern China (Ding and Ke 2015), the criteria we used to identify HWDs in China contains both T_{max} and relative humidity thresholds. An HWD refers to a day with T_{max} exceeding 35°C (Huang et al. 2010) and relative humidity exceeding 60% (Ding and Ke 2015).

According to the 55 summer mean accumulated HWDs based on the aforementioned HWD definition for each grid, YHRB (25° – 35°N , 110° – 122°E) is the center of HW occurrence over China (Fig. 1a). Instead of predicting HWDs on each grid, the accumulated HWDs averaged over the core region in each peak summer (JA) were defined as the predictand in this study, and the time series is shown in Fig. 1b. The HWDs over the YHRB has no significant trend [$0.11 \text{ days (decade)}^{-1}$] but exhibits large year-to-year and decadal variations. This large-scale predictand reduces noise at each grid and facilitates better understanding of the

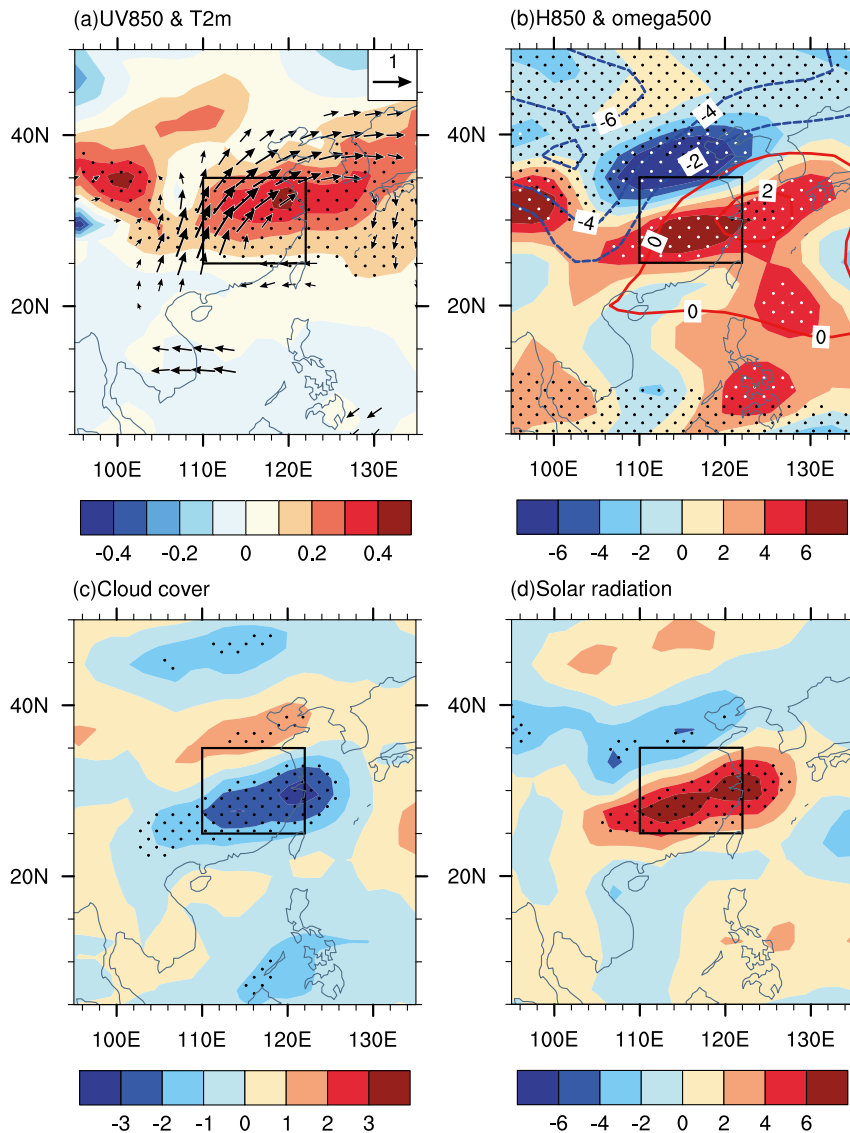


FIG. 2. Simultaneous (JA) atmospheric circulation and temperature anomalies regressed to HWDs averaged over the YHRB. Shown are the regressed (a) 850-hPa wind (vectors; m s^{-1}) and 2-m air temperature (shading; $^{\circ}\text{C}$); (b) 850-hPa geopotential height (contours; gpm) and 500-hPa vertical velocity [shading; $10^{-3} \text{ Pa s}^{-1}$, positive (negative) values denote descending (ascending) motion]; (c) total cloud cover (%); and (d) downward solar radiation (W m^{-2}) anomalies. The black rectangles represent the YHRB. In (a), only the winds significant at the 95% confidence level are shown. Dots indicate where the results are significant at the 95% confidence level [in (b), white and black dots for vertical velocity and geopotential height, respectively].

major physical mechanisms controlling HW occurrence. This integrated predictand is also highly representative of the HWDs at each grid over YHRB as shown by the correlation coefficient map (Fig. 1c).

b. Simultaneous atmospheric circulation associated with the YHRB HWDs

To understand what controls the interannual variability of the total number of HWDs, we first investigated the

HWD-associated atmospheric circulation and temperature anomalies in JA (Figs. 2 and 3). When a low-level anticyclonic (high pressure) anomaly occurs over the YHRB, local surface temperature increases via adiabatic heating resulting from the anomalous descending motion and increased solar radiation caused by the reduced cloud cover (Fig. 2).

The formation of this anticyclonic anomaly over YHRB could be further attributed to the equatorial SST

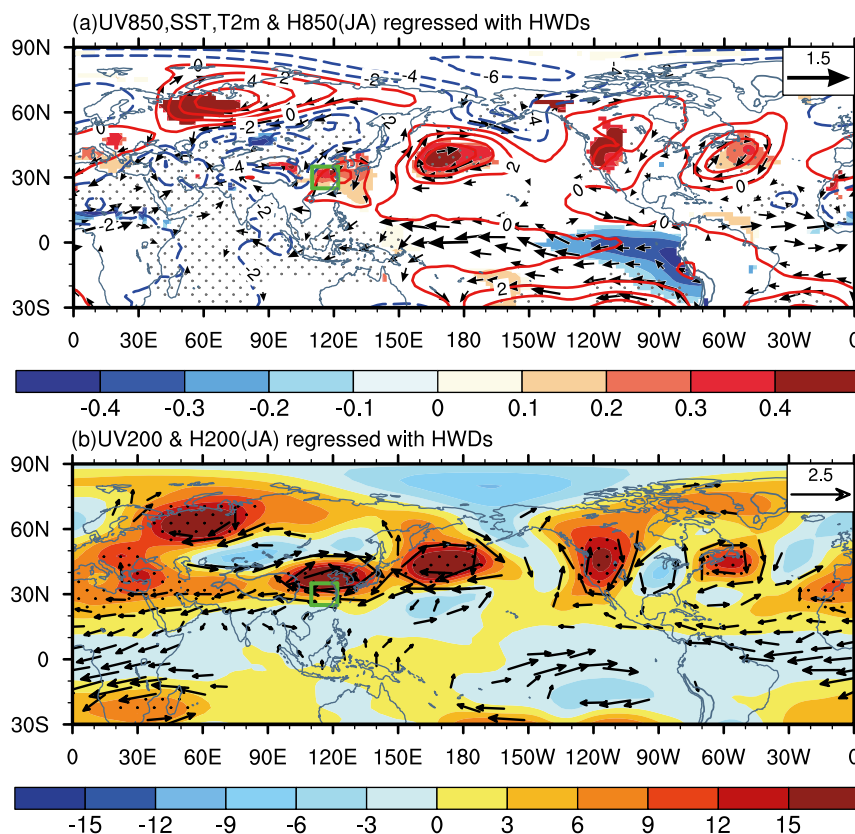


FIG. 3. Simultaneous (JA) atmospheric circulation and temperature anomalies regressed to HWDs averaged over the YHRB. Shown are the regressed (a) 850-hPa wind (vectors; m s^{-1}), SST (shading; $^{\circ}\text{C}$), 2-m air temperature over land (shading; $^{\circ}\text{C}$), and 850-hPa geopotential height (contours, red is positive and blue is negative; gpm) and (b) 200-hPa wind (vectors; m s^{-1}) and 200-hPa geopotential height (shading; gpm) anomalies. The green rectangles represent the YHRB. Only the winds and temperature anomalies significant at the 95% confidence level are shown. Dots indicate the geopotential height anomalies significant at the 95% confidence level.

anomalies over the Pacific and an upper-tropospheric wave train in the mid-to-high latitudes (Fig. 3). On one hand, associated with HWDs, the negative SST anomaly over the equatorial eastern Pacific (EP) and the easterly winds along the equatorial Pacific feature a developing EP La Niña pattern, which could enhance the WPSH and influence the YHRB (Wang et al. 2013) (Fig. 3a). On the other hand, the most prominent characteristic of HWD-related upper-level circulation is a Rossby wave train with a barotropic structure consisting of successive pressure troughs and ridges from Eurasia to North America and the North Atlantic, which is similar to the circumglobal teleconnection (CGT) found by Ding and Wang (2005) (Fig. 3b). The positive centers of this wave train are located over European Russia, East Asia, the North Pacific, North America, and the North Atlantic, contributing to the formation of a low-level anticyclonic anomaly over the YHRB. The features of simultaneous

atmospheric circulation associated with HWDs provide enlightening information for searching for predictors.

4. Predictors for the HWDs over the YHRB

To identify physically meaningful predictors for HWDs over the YHRB, correlation maps between the predictand and the lower-boundary variables (SST, 2-m air temperature over land, and SLP) were examined. We focused on three types of precursors from December to May: seasonal mean (e.g., DJF), short-term tendency (e.g., April–May mean minus February–March mean), and long-term tendency (e.g., April–May mean minus December–January mean). The reasons for selecting these types of predictors have been discussed in previous studies (Yim et al. 2014; Wang et al. 2015).

According to the correlation maps, the two best SST precursory signals during the training period, which are

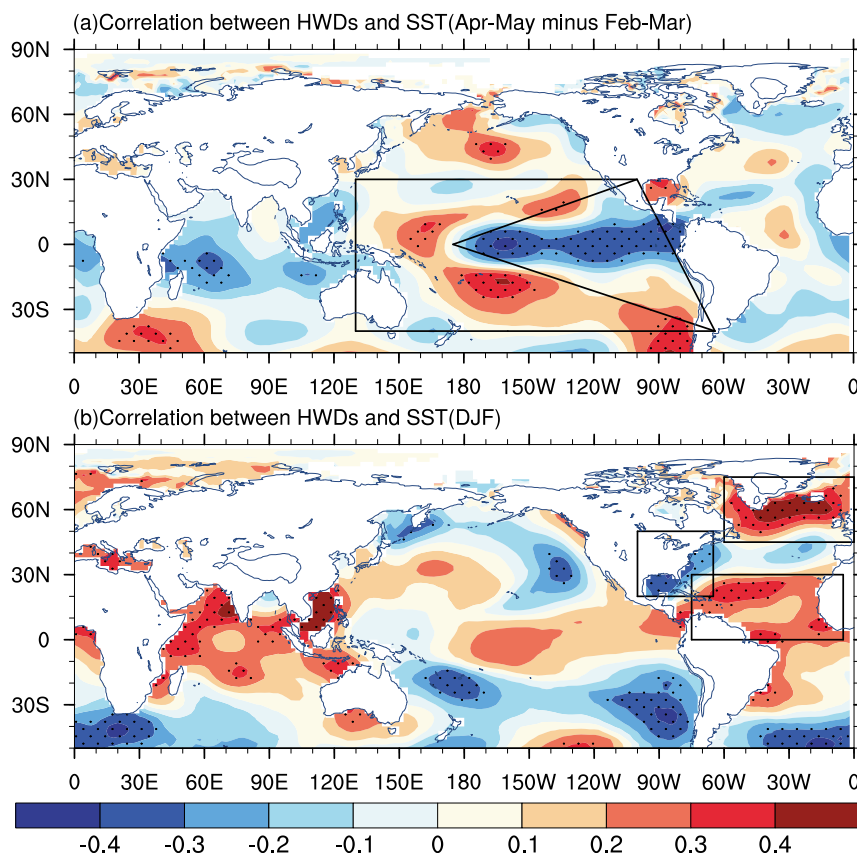


FIG. 4. The correlation maps between integrated HWDs averaged over the YHRB and (a) SST tendency (April–May minus February–March) and (b) SST in DJF. The polygons show the locations used for the EP–SST predictor in (a) and the NA–SST predictor in (b) for HWDs. Dots indicate where the results are significant at the 95% confidence level.

physically connected to and significantly correlated with HWDs over the YHRB, were selected. The first signal is the short-term SST tendency averaged over the western Pacific K-shaped area minus that averaged over the EP triangle at 40°S – 30°N , 130°E – 64°W . Note that the SST tendency was calculated by subtracting the February–March mean SST from the April–May mean SST. The second signal is the SST averaged over 45° – 75°N , 60°W – 0° plus the SST averaged over 0° – 30°N , 75° – 5°W minus the SST averaged over 20° – 50°N , 100° – 65°W in DJF (Fig. 4 and Table 1). Note that only the grids in the defined region that have a correlation coefficient

with the HWDs significant at the 95% confidence level were used.

a. Developing EP La Niña predictor

The first predictor is derived from a short-term tendency of east–west contrasted SST over the Pacific characterized by K-shaped SST warming over the western Pacific and the triangle SST cooling over the EP between February–March and April–May (called the “EP–SST” for brevity) (Fig. 4a). The correlation coefficient of the EP–SST predictor and the HWDs over YHRB is 0.53 (significant at the 99% confidence level).

TABLE 1. The definitions of predictors. Only the grids in the defined region in which correlation coefficients with HWDs are significant at the 95% confidence were used.

Predictor	Month	Definition
EP–SST	April–May minus February–March	SST averaged over the western Pacific K-shaped area at 40°S – 30°N , 130°E – 64°W minus the eastern Pacific triangle at 40°S – 30°N , 175°E – 64°W .
NA–SST	DJF	SST averaged over 45° – 75°N , 60°W – 0° plus SST averaged over 0° – 30°N , 75° – 5°W minus SST averaged over 20° – 50°N , 100° – 65°W .

How can the EP–SST predictor change summer HW occurrence? To address this question, the low-level atmospheric circulation and temperature anomalies regressed to the EP–SST are illustrated in Fig. 5. The results indicate that this zonal dipole SST anomaly implies that the SST pattern will evolve from a decaying central Pacific (CP) El Niño in early spring into a developing EP La Niña in late summer (Figs. 5a,b). In late summer, the significant sea surface cooling over the equatorial CP–EP shifts the Walker circulation westward, which reduces convection along the equatorial CP and enhances convection over the Maritime Continent (Fig. 5c). The suppressed convection over the equatorial CP strengthens the WPSH by the emanation of descending Rossby waves, which has been proposed by Wang et al. (2013). Meanwhile, the enhanced convection over the Maritime Continent produces a high pressure anomaly over southern China through inducing a Pacific–Japan (P–J)/East Asia–Pacific (EAP) teleconnection (Nitta 1987; Huang and Li 1989).

b. North Atlantic Ocean SST predictor

The second predictor is related to a meridional tripole SST pattern over the North Atlantic Ocean in the preceding winter (DJF) with sea surface warming in the low and high latitudes and cooling along the east coast of North America to the Gulf of Mexico (called the “NA–SST” predictor for brevity) (Fig. 4b). The correlation coefficient between the NA–SST predictor and the predictand is 0.54 (significant at the 99% confidence level).

How does this winter tripole SST pattern foreshadow the HWDs over the YHRB in the following summer? First, this tripole SST pattern maintains itself from winter to the following summer over the North Atlantic (Fig. 6a). Previous studies have pointed out that the generation of such a tripole SST pattern over North Atlantic resulted from the North Atlantic Oscillation (NAO)-like atmospheric circulation anomalies with barotropic structure (Watanabe et al. 1999; Pan 2005). A negative NAO phase leads to the equatorward shift of the North Atlantic storm track, accompanied by a dipole cyclonic and anticyclonic anomaly, respectively, located to the north and south of 30°N over the North Atlantic (Fig. 7a). Correspondingly, the high (low) surface wind speed induces negative (positive) SST anomalies, leading to the local tripole SST mode. In turn, this tripole SST pattern could enhance this atmospheric dipole via synoptic eddy forcing (Pan 2005, 2007). Thus, the tripole SST pattern is sustained through this positive air–sea feedback. In addition, to estimate the contribution of ocean memory, which has been reported to play an important role in the maintenance of the tripole SST mode

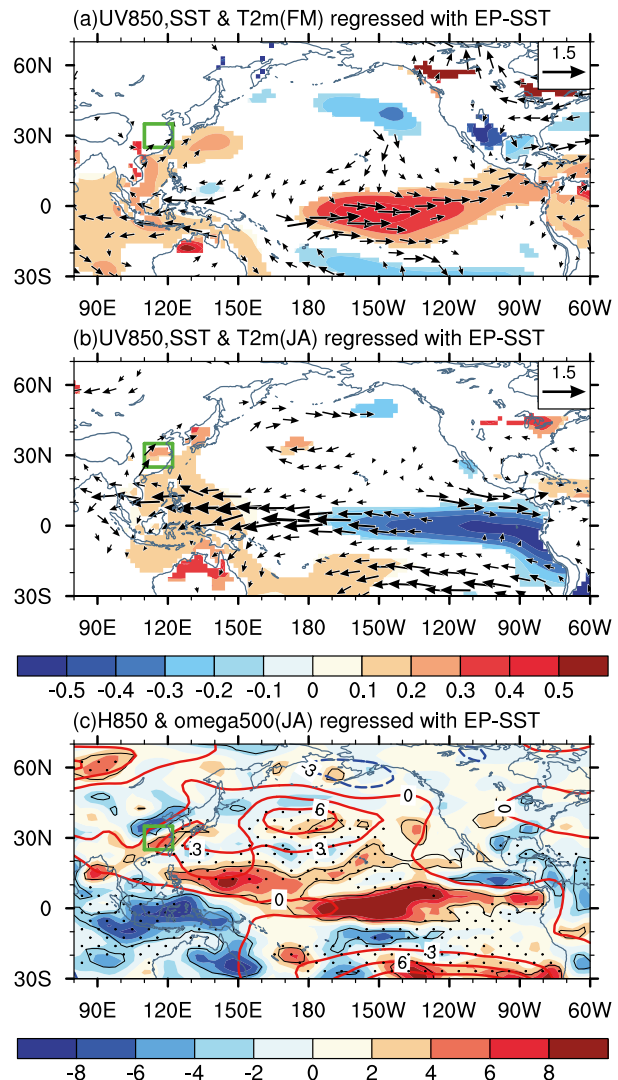


FIG. 5. Atmospheric circulation and temperature anomalies regressed to EP–SST predictor. Shown are the regressed (a), (b) 850-hPa wind (vectors; m s^{-1}), SST (shading; $^{\circ}\text{C}$), and 2-m air temperature over land (shading; $^{\circ}\text{C}$) and (c) 850-hPa geopotential height (contours; gpm) and 500-hPa vertical velocity (shading; $10^{-3} \text{ Pa s}^{-1}$) anomalies for February–March in (a) and July–August in (b), (c). The green rectangles represent the YHRB. In (a), (b), only the wind anomalies significant at the 95% confidence level are shown. Dots and the black contours indicate the geopotential height and temperature anomalies significant at the 95% confidence level, respectively.

over the North Atlantic in spring (Wu et al. 2009), we investigated the persistent component of SST from winter to summer according to Pan (2005) (Fig. 6b). The formula could be written as $\text{SST}_p = \text{SST}(t) \text{Cov}[\text{SST}(t+1), \text{SST}(t)] / \text{Var}[\text{SST}(t)]$, where $t+1$ and t denote the summer (JA) and the preceding winter [December–February (DJF)], respectively; and Cov and Var represent the covariance and variance functions, respectively. Compared to summer SST anomalies, the SST persistent

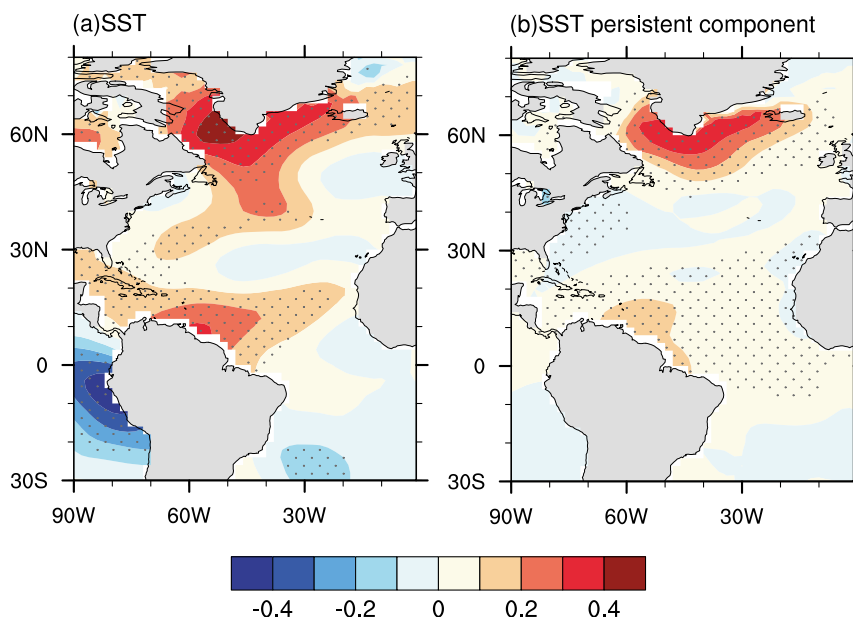


FIG. 6. (a) SST anomalies (shading; $^{\circ}\text{C}$) and (b) SST persistent component regressed to NA-SST predictor in JA. Dots indicate where the results are significant at the 95% confidence level.

component captures the feature of the tripole mode with decreased amplitudes (Fig. 6), which confirms the contribution of ocean memory. Therefore, both the positive air–sea feedback and ocean memory effect can

account for the persistence of this winter predictor to the following summer.

In late summer, this tripole SST pattern excites a CGT-like wave train with a barotropic structure

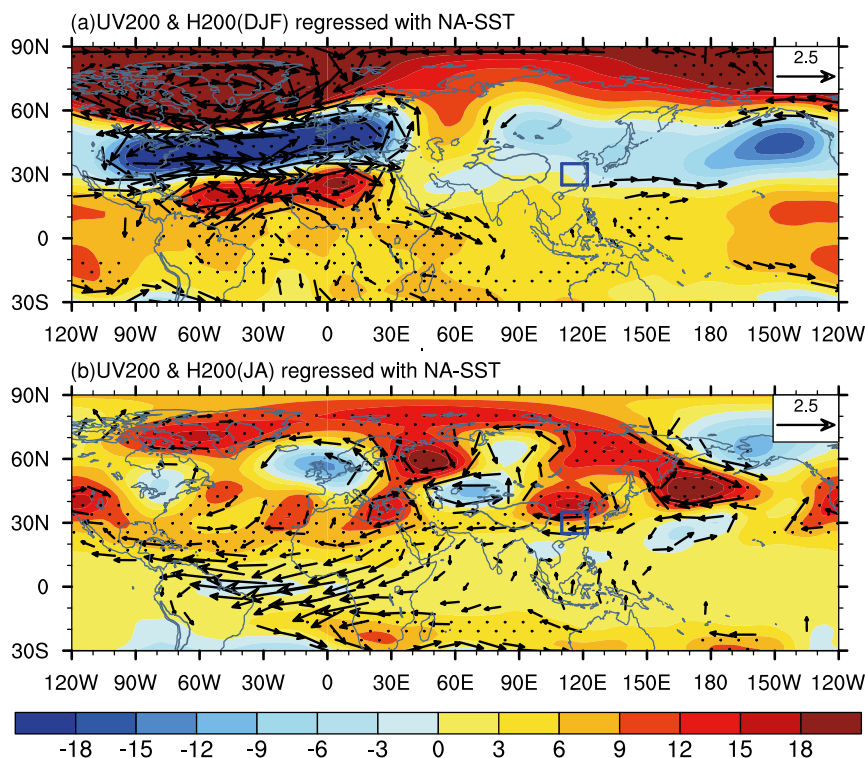


FIG. 7. The 200-hPa wind (vectors; m s^{-1}) and geopotential height (shading; gpm) anomalies regressed to NA-SST predictor in (a) DJF and (b) JA. The blue rectangles represent the YHRB. Dots indicate where the results are significant at the 95% confidence level. Only the wind anomalies significant at the 95% confidence level are shown.

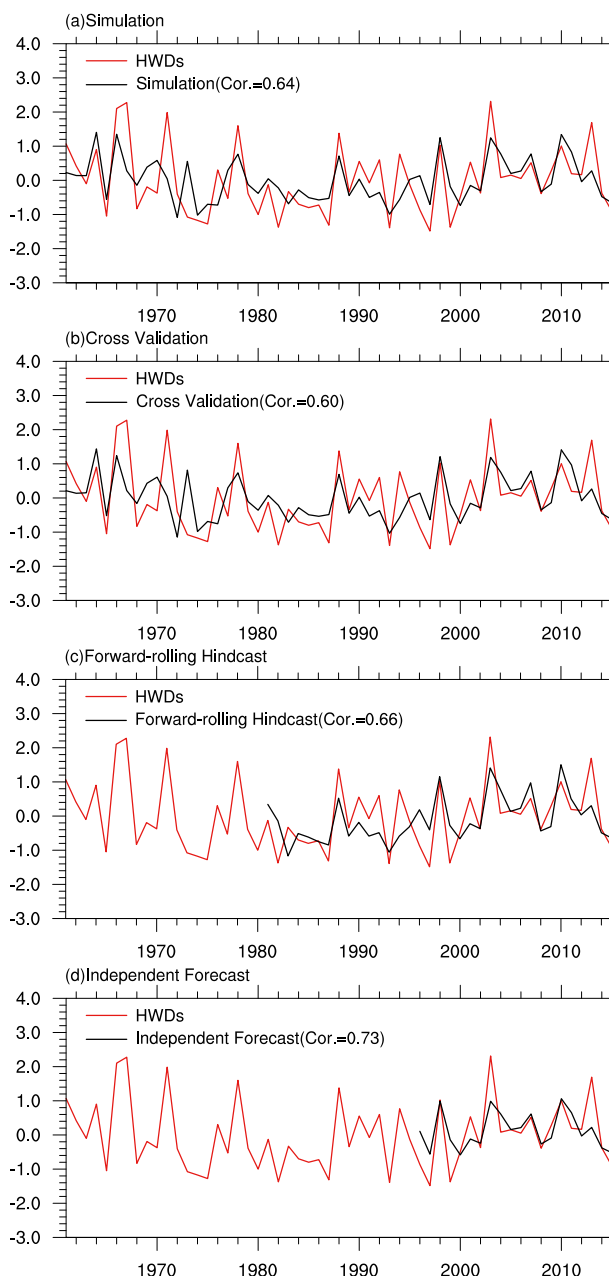


FIG. 8. Prediction skills of the PEM for accumulated HWDs averaged over the YHRB. Time series of normalized observed HWDs without removing the long-term trend (red) and (a) simulated HWDs in 1961–2015 (black), (b) cross-validated HWDs in 1961–2015 (black), (c) forward-rolling hindcast of HWDs in 1981–2015 (black), and (d) independent forecast of HWDs in 1996–2015 (black).

(Fig. 7b). According to the observation and numerical experiment by Wu et al. (2009), the tripole SST mode could influence East Asia by inducing the downstream development of subpolar teleconnections across northern Eurasia in summer. Meanwhile, the CGT could also be stimulated by the enhanced Indian summer monsoon

rainfall (Ding et al. 2011), which was found to be related to the tripole SST pattern over the North Atlantic (figure not shown). In addition, the internal dynamics of basic flow contributes to the formation and maintenance of the CGT (Ding et al. 2011).

As a result, the high pressure centers along this wave train appear over European Russia, East Asia, the western North Pacific, North America, and the North Atlantic Ocean. The positive center located over East Asia influences the YHRB and contributes to the increase of HWDs.

5. Estimation of the HWDs' predictability over the YHRB

How predictable are HWDs over the YHRB by using the two predictors we selected? To address this question, we established a PEM with a regression method with the HWDs being the predictand. The simulation equation derived from the training period of 1961–2015 is $\text{HWDs} = 0.377 \times \text{EP-SST} + 0.388 \times \text{NA-SST}$. The prediction skill of this PEM for 55 years could reach 0.64 (significant at the 99% confidence level) (Fig. 8a).

We applied three types of validation skills to estimate if the prediction model can well predict the HWDs (section 2). As shown in Figs. 8b–d, the PEM produces a cross-validated forecast skill of 0.60 for 1961–2015, a forward-rolling hindcast skill of 0.66 for 1981–2015, and an independent forecast skill of 0.73 for 1996–2015 (Table 2). According to the forward-rolling hindcast, about 55% of the total variance of the HWDs over the YHRB are potentially predictable.

The abovementioned two physical predictors can also be used to forecast the accumulated days of HW events (HWEDs) which refers to the processes with equal or more than three consecutive HW days. The regression equation for the HWEDs over the YHRB established with EP-SST and NA-SST predictors for 1961–2015 is $\text{HWEDs} = 0.386 \times \text{EP-SST} + 0.377 \times \text{NA-SST}$. The simulation, cross-validated forecast, forward-rolling hindcast, and independent forecast skill are 0.64, 0.65, and 0.74, respectively (Table 2).

6. Summary and discussion

This study identifies the core region of sultry HWDs in China and obtains the time series of total number of HWDs averaged over the YHRB. Two physical precursors for HW occurrence were selected based on the correlation maps between HWDs over the YHRB and the lower-boundary variables from December to May, which indicate the source of predictability of HWDs. The first one is a zonal dipole SST tendency in the

TABLE 2. The prediction skills (correlation coefficients) of the PEM for HWDs and HWEDs over the YHRB. All values are statistically significant at the 99% confidence level.

Correlation coef	Simulation (1961–2015)	Cross-validated forecast (1961–2015)	Forward-rolling hindcast (1981–2015)	Independent forecast (1996–2015)
HWDs	0.64	0.60	0.66	0.73
HWEDs	0.64	0.60	0.65	0.74

Pacific, which reflects a rapid transition from a decaying CP El Niño in early spring to a developing EP La Niña in late summer. The EP La Niña-induced sea surface cooling over the CP modifies the Walker circulation, which enhances the WPSH through exciting descending Rossby wave and P-J/EAP teleconnection, resulting in increased HWDs over the YHRB. Another predictor is a persistent meridional tripole SST pattern over the North Atlantic in winter, which persists till the following summer through positive air–sea feedback and ocean memory and excites a barotropic CGT-like wave train with a high pressure center over the YHRB.

According to the two SST predictors mentioned above, a 1-month lead PEM for HWDs over the YHRB was established. The simulation skill reaches 0.64 for the entire 55-yr period. This PEM prediction can produce a cross-validated forecast skill of 0.60 for 1961–2015, a forward-rolling hindcast skill of 0.66 for 1981–2015, and an independent forecast skill of 0.73 for 1996–2015. The results indicate that about 55% of the total variance of HWDs are potentially predictable, which provides an estimate for the lower bound of HWDs' predictability and implies there exists great potential for the improvement of dynamical prediction.

The causative processes of the low-level anticyclone over the YHRB favoring the predictors and predictand we proposed have been supported by the results of some numerical experiments in previous studies, including the strengthening of the WPSH by La Niña-associated SST via emanating descending Rossby wave and P-J/EAP teleconnection (e.g., Huang and Li 1989; Wang et al. 2013) and the contribution of the air–sea interaction to the maintenance of the NA–SST predictor over the North Atlantic from winter to the following summer (Pan 2007). However, although the linkage between the summer tripole SST mode over the North Atlantic and downstream teleconnections across northern Eurasia has been reproduced by a numerical model (Wu et al. 2009) and the processes of CGT generation have been discussed in detail by Ding et al. (2011), how the tripole SST mode induces CGT needs further investigation via well-designed numerical experiments.

It is also worth noting that the two predictors used in this study exhibit decadal variability. First, the relationship

between HWDs and the EP–SST predictor had abruptly changed around the late 1970s [i.e., their correlation coefficient increased from 0.36 (not significant) into 0.66 (significant at the 99% confidence level) after 1979 (figure not shown)]. Correspondingly, the prediction skill for the HWDs (0.70) after the late 1970s is higher than before (0.55). This decadal change might be ascribed to the abrupt change of SST over Pacific Ocean around the late 1970s that has been widely reported (e.g., Wang and An 2001; Meehl et al. 2009; Jia et al. 2014). Second, the relationship between HWDs and NA–SST predictor after the late 1990s becomes better (the correlation coefficient after 1998 between them is 0.55) than before 1998 (0.50). The combined effect of two predictors leads to a higher independent forecast skill (0.73) than only simulation (0.64). Therefore, the prediction skill of the PEM may change with a different training period. The results also indicate that a PEM built with multipredictors linked to a predictand through different physical processes will have a more stable prediction skill.

Using different HW definitions, we found another interesting result is that the ratio of sultry HWDs to the total HWDs (defined as accumulated days with T_{\max} exceeding 35°C) over the YHRB decreases after the early 2000s, while the ratio of dry HWDs (defined as accumulated days with T_{\max} exceeding 35°C and relative humidity below 60%) increases (Fig. 9). According to the Lepage test (Lepage 1971), the percentage of wet HWDs significantly decreases from 97.4% in 1961–2002 to 88.4% after 2002, which indicates that HWs over

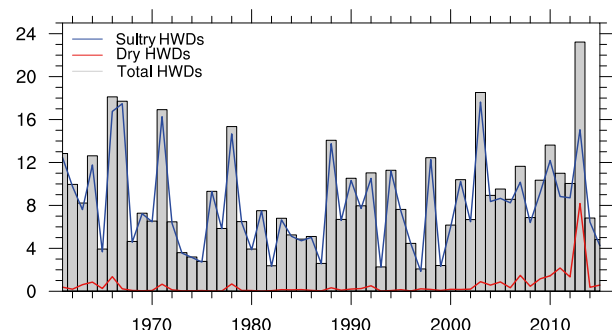


FIG. 9. Time series of the accumulated sultry HWDs (blue), dry HWDs (red), and total HWDs (gray bars) averaged over the YHRB for 1961–2015.

YHRB become drier after the early 2000s. Since sultry HWs have a great impact on human health, the reason for the decadal change is worth investigating.

Acknowledgments. Miaoni Gao and Jing Yang were supported by funds from the National Key Research and Development Program-Global Change and Mitigation Project: Global Change Risk of Population and Economic System: Mechanism and Assessment (Grant 2016YFA0602401) and the National Natural Science Foundation of China (Grants 41775071 and 41621061). Bin Wang acknowledges the support from the National Natural Science Foundation of China (Grant 41420104002) and the National Research Foundation (NRF) of Korea through a Global Research Laboratory (GRL) grant of the Korean Ministry of Education, Science and Technology (MEST; 2011-0021927). This study was supported by the National Key Research and Development Program project 2016YFA0602503. This is the NUIST-Earth System Modeling Center Publication 198, the School of Ocean and Earth Science and Technology Publication 10282, and the International Pacific Research Center Publication 1298.

REFERENCES

- Anderson, G. B., and M. L. Bell, 2011: Heat waves in the United States: Mortality risk during heat waves and effect modification by heat wave characteristics in 43 U.S. communities. *Environ. Health Perspect.*, **119**, 210–218, <https://doi.org/10.1289/ehp.1002313>.
- Ding, Q. H., and B. Wang, 2005: Circumglobal teleconnection in the Northern Hemisphere summer. *J. Climate*, **18**, 3483–3505, <https://doi.org/10.1175/JCLI3473.1>.
- , —, J. M. Wallace, and G. Branstator, 2011: Tropical–extratropical teleconnections in boreal summer: Observed interannual variability. *J. Climate*, **24**, 1878–1896, <https://doi.org/10.1175/2011JCLI3621.1>.
- Ding, T., and Z. Ke, 2015: Characteristics and changes of regional wet and dry heat wave events in China during 1960–2013. *Theor. Appl. Climatol.*, **122**, 651–665, <https://doi.org/10.1007/s00704-014-1322-9>.
- Easterling, D. R., G. A. Meehl, C. Parmesan, S. A. Changnon, T. R. Karl, and L. O. Mearns, 2000: Climate extremes: Observations, modeling, and impacts. *Science*, **289**, 2068–2074, <https://doi.org/10.1126/science.289.5487.2068>.
- Gao, M. N., J. Yang, B. Wang, S. Y. Zhou, D. Y. Gong, and S.-J. Kim, 2018: How are heat waves over Yangtze River valley associated with atmospheric quasi-biweekly oscillation? *Climate Dyn.*, <https://doi.org/10.1007/s00382-017-3526-z>, in press.
- Hamilton, E., R. Eade, R. J. Graham, A. A. Scaife, D. M. Smith, A. Maidens, and C. MacLachlan, 2012: Forecasting the number of extreme daily events on seasonal timescales. *J. Geophys. Res.*, **117**, D03114, <https://doi.org/10.1029/2011JD016541>.
- Huang, B. Y., and Coauthors, 2015: Extended Reconstructed Sea Surface Temperature (ERSST), version 4. NOAA National Centers for Environmental Information, accessed 10 September 2016, <https://doi.org/10.7289/V5KD1VVF>.
- Huang, R. H., and L. Li, 1989: Numerical simulation of the relationship between the anomaly of subtropical high over East Asia and the convective activities in the western tropical Pacific. *Adv. Atmos. Sci.*, **6**, 202–214, <https://doi.org/10.1007/BF02658016>.
- Huang, W., H. D. Kan, and S. Kovats, 2010: The impact of the 2003 heat wave on mortality in Shanghai, China. *Sci. Total Environ.*, **408**, 2418–2420, <https://doi.org/10.1016/j.scitotenv.2010.02.009>.
- IPCC, 2013: *Climate Change 2013: The Physical Science Basis*. Cambridge University Press, 1535 pp., <https://doi.org/10.1017/CBO9781107415324>.
- Jia, X. J., J. Y. Lee, H. Lin, A. Alessandri, and K. J. Ha, 2014: Interdecadal change in the Northern Hemisphere seasonal climate prediction skill: Part I. The leading forced mode of atmospheric circulation. *Climate Dyn.*, **43**, 1595–1609, <https://doi.org/10.1007/s00382-013-1988-1>.
- Kalnay, E., and Coauthors, 1996: The NCEP/NCAR 40-Year Reanalysis Project. *Bull. Amer. Meteor. Soc.*, **77**, 437–471, [https://doi.org/10.1175/1520-0477\(1996\)077<0437:TNYRP>2.0.CO;2](https://doi.org/10.1175/1520-0477(1996)077<0437:TNYRP>2.0.CO;2).
- Lei, Y. N., D. Y. Gong, Z. Y. Zhang, D. Guo, and X. Z. He, 2009: Spatial-temporal characteristics of high-temperature events in summer in eastern China and the associated atmospheric circulation (in Chinese). *Geogr. Res.*, **28**, 653–662.
- Lepage, Y., 1971: A combination of Wilcoxon's and Ansari-Bradleys statistics. *Biometrika*, **58**, 213–217, <https://doi.org/10.1093/biomet/58.1.213>.
- Meehl, G. A., A. X. Hu, and B. D. Santer, 2009: The mid-1970s climate shift in the Pacific and the relative roles of forced versus inherent decadal variability. *J. Climate*, **22**, 780–792, <https://doi.org/10.1175/2008JCLI2552.1>.
- Michaelsen, J., 1987: Cross-validation in statistical climate forecast models. *J. Climate Appl. Meteor.*, **26**, 1589–1600, [https://doi.org/10.1175/1520-0450\(1987\)026<1589:CVISCF>2.0.CO;2](https://doi.org/10.1175/1520-0450(1987)026<1589:CVISCF>2.0.CO;2).
- National Academies of Sciences, Engineering, and Medicine, 2016: *Attribution of Extreme Weather Events in the Context of Climate Change*. National Academies Press, 186 pp., <https://doi.org/10.17226/21852>.
- Nitta, T., 1987: Convective activities in the tropical western Pacific and their impact on the Northern Hemisphere summer circulation. *J. Meteor. Soc. Japan*, **65**, 373–390, https://doi.org/10.2151/jmsj1965.65.3_373.
- NOAA/OAR/ESRL PSD, 1996: NCEP/NCAR reanalysis monthly means and other derived variables. NOAA/Earth System Research Laboratory, accessed 10 September 2016, <https://www.esrl.noaa.gov/psd/data/gridded/data.ncep.reanalysis.derived.surfaceflux.html>.
- Pan, L. L., 2005: Observed positive feedback between the NAO and the North Atlantic SSTA tripole. *Geophys. Res. Lett.*, **32**, L06707, <https://doi.org/10.1029/2005GL022427>.
- , 2007: Synoptic eddy feedback and air-sea interaction in the North Atlantic region. *Climate Dyn.*, **29**, 647–659, <https://doi.org/10.1007/s00382-007-0256-7>.
- Pepler, A. S., L. B. Díaz, C. Prodhomme, F. J. Doblas-Reyes, and A. Kumar, 2015: The ability of a multi-model seasonal forecasting ensemble to forecast the frequency of warm, cold and wet extremes. *Wea. Climate Extremes*, **9**, 68–77, <https://doi.org/10.1016/j.wace.2015.06.005>.
- Smith, T. T., B. F. Zaitchik, and J. M. Gohlke, 2013: Heat waves in the United States: Definitions, patterns and trends. *Climatic Change*, **118**, 811–825, <https://doi.org/10.1007/s10584-012-0659-2>.
- Sun, J.-Q., 2012: Possible impact of the summer North Atlantic Oscillation on extreme hot events in China. *Atmos. Oceanic Sci. Lett.*, **5**, 231–234, <https://doi.org/10.1080/16742834.2012.11446996>.

- Teng, H., G. Branstator, H. Wang, G. A. Meehl, and W. M. Washington, 2013: Probability of US heat waves affected by a subseasonal planetary wave pattern. *Nat. Geosci.*, **6**, 1056–1061, <https://doi.org/10.1038/ngeo1988>.
- Vitart, F., and Coauthors, 2015: The Subseasonal to Seasonal (S2S) Prediction Project. European Centre for Medium-Range Weather Forecasts, accessed 27 September 2017, <http://apps.ecmwf.int/datasets/data/s2s-realtime-instantaneous-accum-ecmf/levtype=sfc/type=cf/>.
- , and Coauthors, 2017: The Subseasonal to Seasonal (S2S) Prediction Project Database. *Bull. Amer. Meteor. Soc.*, **98**, 163–173, <https://doi.org/10.1175/BAMS-D-16-0017.1>.
- Wang, B., and S. I. An, 2001: Why the properties of El Niño changed during the late 1970s. *Geophys. Res. Lett.*, **28**, 3709–3712, <https://doi.org/10.1029/2001GL012862>.
- , J. Liu, J. Yang, T. J. Zhou, and Z. W. Wu, 2009a: Distinct principal modes of early and late summer rainfall anomalies in East Asia. *J. Climate*, **22**, 3864–3875, <https://doi.org/10.1175/2009JCLI2850.1>.
- , and Coauthors, 2009b: Advance and prospectus of seasonal prediction: Assessment of the APCC/CliPAS 14-model ensemble retrospective seasonal prediction (1980–2004). *Climate Dyn.*, **33**, 93–117, <https://doi.org/10.1007/s00382-008-0460-0>.
- , B. Q. Xiang, and J. Y. Lee, 2013: Subtropical High predictability establishes a promising way for monsoon and tropical storm predictions. *Proc. Natl. Acad. Sci. USA*, **110**, 2718–2722, <https://doi.org/10.1073/pnas.1214626110>.
- , —, J. Li, P. J. Webster, M. N. Rajeevan, J. Liu, and K. J. Ha, 2015: Rethinking Indian monsoon rainfall prediction in the context of recent global warming. *Nat. Commun.*, **6**, 7154, <https://doi.org/10.1038/ncomms8154>.
- Watanabe, M., M. Kimoto, T. Nitta, and M. Kachi, 1999: A comparison of decadal climate oscillations in the North Atlantic detected in observations and a coupled GCM. *J. Climate*, **12**, 2920–2940, [https://doi.org/10.1175/1520-0442\(1999\)012<2920:ACODCO>2.0.CO;2](https://doi.org/10.1175/1520-0442(1999)012<2920:ACODCO>2.0.CO;2).
- Wu, J., and X. J. Gao, 2013: A gridded daily observation dataset over China region and comparison with the other datasets (in Chinese). *Chin. J. Geophys.*, **56**, 1102–1111.
- Wu, Z. W., B. Wang, J. P. Li, and F. F. Jin, 2009: An empirical seasonal prediction model of the east Asian summer monsoon using ENSO and NAO. *J. Geophys. Res.*, **114**, D18120, <https://doi.org/10.1029/2009JD011733>.
- , P. Zhang, H. Chen, and Y. Li, 2016: Can the Tibetan Plateau snow cover influence the interannual variations of Eurasian heat wave frequency? *Climate Dyn.*, **46**, 3405–3417, <https://doi.org/10.1007/s00382-015-2775-y>.
- Xu, Y., X. J. Gao, Y. Shen, C. H. Xu, Y. Shi, and F. Giorgi, 2009: A daily temperature dataset over China and its application in validating a RCM simulation. *Adv. Atmos. Sci.*, **26**, 763–772, <https://doi.org/10.1007/s00376-009-9029-z>.
- Yim, S.-Y., B. Wang, and W. Xing, 2014: Prediction of early summer rainfall over South China by a physical-empirical model. *Climate Dyn.*, **43**, 1883–1891, <https://doi.org/10.1007/s00382-013-2014-3>.
- You, Q. L., Z. H. Jiang, L. Kong, Z. W. Wu, Y. T. Bao, S. C. Kang, and N. Pepin, 2016: A comparison of heat wave climatologies and trends in China based on multiple definitions. *Climate Dyn.*, **48**, 3975–3989, <https://doi.org/10.1007/s00382-016-3315-0>.
- Zhang, J. Y., and L. Y. Wu, 2011: Land-atmosphere coupling amplifies hot extremes over China. *Chin. Sci. Bull.*, **56**, 3328–3332, <https://doi.org/10.1007/s11434-011-4628-3>.
- Zhou, Y. F., and Z. W. Wu, 2016: Possible impacts of mega-El Niño/Southern Oscillation and Atlantic Multidecadal Oscillation on Eurasian heatwave frequency variability. *Quart. J. Roy. Meteor. Soc.*, **142**, 1647–1661, <https://doi.org/10.1002/qj.2759>.